



Journal Name

COMMUNICATION

## Understanding quaternary compound $\text{Cu}_2\text{ZnSnSe}_4$ synthesis by microscopic scale analyses at an identical location

Received 00th January 20xx,  
Accepted 00th January 20xx

A. Crossay<sup>a†</sup>, D. Colombara<sup>a†</sup>, M. Melchiorre<sup>a</sup>, M. Guennou<sup>b</sup>, B.G. Mendis<sup>c</sup>, P. J. Dale<sup>a†</sup>

DOI: 10.1039/x0xx00000x

www.rsc.org/

**The synthesis of multinary compound films from layered precursors is only partially understood. Identical location microscopy resolves the multi-step synthesis of  $\text{Cu}_2\text{ZnSnSe}_4$  from metallic stacks on the micron-scale. Large scale metal alloying and the seemingly illogical observation that ZnSe segregates preferentially on locations previously poor of zinc are revealed.**

As society's energy needs increase, scientists are urged to find sustainable solutions to such demands. Therefore, attention tends to move from single to multi-component systems, promising ever greater performance at the price of an increased complexity<sup>1</sup>. Multinary compounds offer the possibility to adapt the chemical and physical properties of materials to the constraints required by technology and/or the environment, but this may come with limited degrees of freedom. For applications where chemical purity is crucial to attain suitable device functionality, it is key to understand the chemical reactions involved during the synthesis, in order to avoid potential secondary phase segregation mechanisms.

A case study is represented by the semiconductor  $\text{Cu}_2\text{ZnSn}(\text{S},\text{Se})_4$  Kesterite, which is investigated as an absorber material for thin film photovoltaic devices<sup>2</sup>. This compound offers a very promising alternative to current technologies mainly based on CdTe and  $\text{Cu}(\text{In},\text{Ga})\text{Se}_2$ , since it does not contain scarce elements such as In, Ga or Te<sup>3</sup>, and 12.6 % efficient solar cells have already been demonstrated<sup>4</sup>. However, synthesis of Kesterite is challenging as it is a quaternary compound, which raises problems of formation and segregation of deleterious binary or ternary chalcogenide phases that reduce device performance<sup>5</sup>. In this study we follow the 2-stage synthesis process<sup>6</sup> commonly applied to semiconductors such as  $\text{Cu}(\text{In},\text{Ga})(\text{S},\text{Se})_2$ ,  $\text{Cu}_2\text{ZnSn}(\text{S},\text{Se})_4$  and  $\text{Cu}_2(\text{Sn},\text{Ge})\text{S}_3$  i.e. deposition of a metal precursor film, followed by a reactive thermal treatment to incorporate sulfur and/or

selenium<sup>2,7–9</sup>. For the fabrication of  $\text{Cu}_2\text{ZnSnSe}_4$  Kesterite, our modified version of this process involves (i) the sequential electrodeposition of Cu, Sn and Zn on Mo-coated glass substrates, followed by (ii) a soft-annealing step at 350°C in inert atmosphere<sup>10,11</sup>, followed by (iii) a gas-phase selenization step at 525°C to allow Kesterite formation. Step (ii) stabilizes the precursors from uncontrolled metal alloying before the selenization process. This intermixing of the precursor elements normally goes unseen when proceeding directly from step (i) to (iii): at the beginning of step (iii) the metals alloy, as the metallic precursor is heated and the selenium vapour pressure is too low to selenize the metals. With our three step procedure we attained a maximum device power conversion efficiency of 7 %, which is comparable to the best reported device of 8.2 % fabricated similarly<sup>12</sup>. The best Kesterite devices consist of absorber layers grown with a copper poor and zinc rich composition, which leads inevitably to the presence of a ZnSe secondary phase. It is believed that Kesterite films without large ZnSe segregation can attain even higher power conversion efficiencies<sup>13</sup>.

Secondary phase segregation in these chalcogenide systems occurs usually on the micron scale. In order to understand their mechanism of formation and segregation at this scale, commonly used techniques such as x-ray diffraction (XRD) and macroscopic Raman are of modest use, since the information they provide is averaged over length scales larger than the segregation size. Ideally, in-situ micron-scale spatially resolved analysis is required during each process step.

However, traditional in-situ electron microscopy analyses<sup>14–16</sup> cannot be easily implemented, because of the corrosive selenium gas used in the synthesis. Very interesting in-situ XRD analyses were reported<sup>17,18</sup> to study specifically the Kesterite phase formation, but due to the large beam area no spatially-resolved information is obtainable.

<sup>a</sup> Physics and Materials Science Research Unit, Université du Luxembourg, 41, rue du Brill, L-4422 Belvaux, Luxembourg

<sup>b</sup> Luxembourg Institute of Science and Technology, 41, rue du Brill, L-4422 Belvaux, Luxembourg

<sup>c</sup> Department of Physics—Durham University, Durham DH13LE, United Kingdom

† Corresponding authors are alexandre.crossay@uni.lu, diego.colombara@uni.lu and phillip.dale@uni.lu

Electronic Supplementary Information (ESI) available: sample preparation and methods. See DOI: 10.1039/x0xx00000x

The present study demonstrates an alternative ex-situ strategy that identifies a specific location on a sample by a simple marking of its surface, and to retrieve it after each process step performed on the sample. These specific sample and location are referred to as “sample of interest”, and “area of interest” in the following. Morphological and mapping analyses (SEM-EDX, micro-photoluminescence (PL)/Raman) are performed on this area of interest and provide the desired micron-scale 2-D spatial information. Combining this feature with the (discontinuous) temporal information allows the technique to approach the efficacy of a time-resolved 2-D in-situ analysis. Detailed experimental methods are given in the supplementary information †. Similar positioning techniques have been successfully employed to follow liquid phase reactions at the surface of electrodes<sup>19</sup> and semiconductors<sup>20</sup>.

After step (i), the electrodeposited Cu/Sn/Zn layer stack shows good morphological and compositional lateral uniformity, as seen by the SEM image and corresponding Zn molar ratio composition map in Figures 1a and 2a for a sample grown under the exact same conditions as the sample of interest. The only observable microstructural features have a size of less than one micron and no strong lateral chemical gradients are observable. However, since the metal deposition is sequential, the films do have a strong vertical compositional gradient (the stack is composed of 200 nm Cu, 240 nm Sn, 180 nm Zn). When such a stack is used, it was shown by Ahmed et al.<sup>10</sup> and explained by Arasimowicz et al.<sup>11</sup> that a soft annealing step under inert atmosphere leads to the formation of micron sized columnar Cu-Zn and Cu-Sn alloys. Interdiffusion of metals to form these alloys is a process driven by the formation of more stable intermetallic bonds, and the binary system observed is consistent with the absence of known ternary alloys at this temperature<sup>21</sup>. It was shown that thanks to this soft annealing process, more uniform and less rough<sup>22</sup> Kesterite films can be obtained after the selenization step, leading to higher device efficiency<sup>23</sup>.

Figure 1b) shows a top view SEM image of the position of interest after soft annealing at 350°C for 30 min. Two distinct regions are clearly observed: 10-20 μm sized dark islands (region 1) surrounded by a brighter area (region 2). As seen on a cross section of a sister sample fig 1d.ii), region 1 appears single phase and compositionally homogeneous in-depth, we call this “phase 1”. Region 2 on the other hand, seems constituted of a second phase (phase 2) along with particles of phase 1. Grazing incidence XRD measurements clearly show the presence of Cu<sub>5</sub>Zn<sub>8</sub> and Sn phases (figure 1c). The additional presence of CuZn and Cu<sub>6</sub>Sn<sub>5</sub> is possible, but not certain due to the combination of overlapping peaks with other phases and the absence of minor peaks in the diffractogram. An EDX map was made on the area of interest to identify the composition of the two regions. From these measurements, molar fractions of Zn, Cu<sub>2</sub> and Sn are calculated and their distributions are displayed as maps in figures 2c), 2d) and 2e). The zinc and copper maps show a clear compositional anti-correlation with respect to the tin map, and we assign region 1 and 2 respectively to Sn-poor and Sn-rich

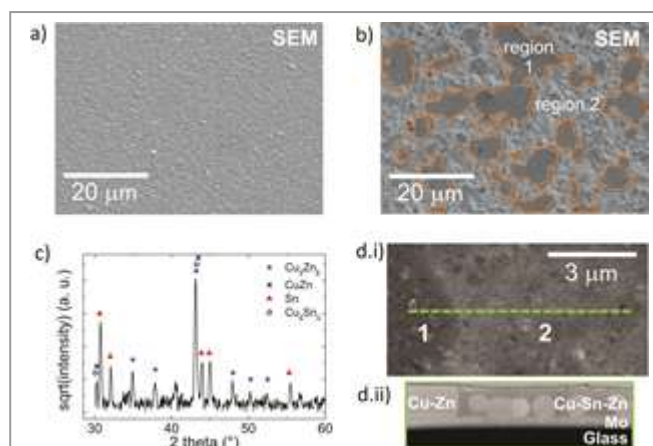


Figure 1: SEM top view images of a) typical sample as deposited, and b) position of interest after 350°C soft annealing, with orange contour lines defined by a Sn molar ratio of Sn<0.25 (see figure 2d); c) GIXRD of the sample of interest. Figure d.i) is a top view SEM image of a soft annealed sister sample; a cross section image of this is cut along the green dashed line and is shown in d.ii).

areas. The demarcation between the two regions is highlighted by a contour line to aid discussion throughout the paper.

Figure 2b) provides an overview of all compositions in the area of interest on the Cu<sub>2</sub>-Zn-Sn ternary diagram. The green oval delimits the as electrodeposited (former) composition, which is much smaller compared to the composition spread after soft annealing, confirming that a strong lateral inhomogeneity in composition occurs during step (ii). A clear

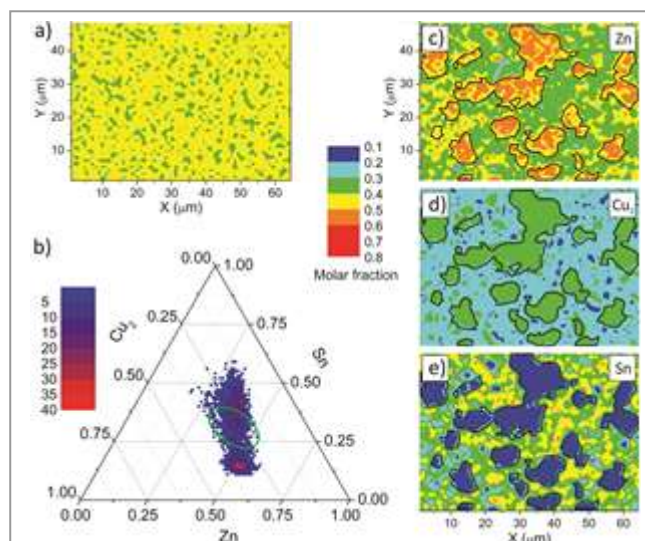


Figure 2: Chemical map displaying molar ratios of a) zinc of a typical as deposited sample, and of c), d) and e) respectively zinc, copper and tin on position of interest after soft annealing. Each map is overlaid with the orange contour lines of figure 1b) now displayed in black. Figure 2b) displays the ternary compositions of every point of the soft annealed position of interest, each composition being color-coded to represent the number of occurrences with the same composition. The green oval shows the former limit of spread of compositions of the as deposited sample.

bimodal distribution of compositions is revealed as well, consistent with the compositional maps. The Sn-poor compositions centred on (0.34 Cu<sub>2</sub>, 0.15 Sn), (corresponding mostly to the phase β'CuZn(5%Sn) according to the 250°C phase diagram<sup>21</sup>) are attributed to region 1 and phase 1 of the SEM image in figure 1b). The second type of composition detected is attributed to region 2. It is more Sn-rich and is compositionally broader than region 1 (from Sn 0.25 to Sn 0.5), which is consistent with the FIB cross section image (Fig 1d.ii) and EDS cross section analyses (supporting information, figure S12) showing inclusions of a Cu-Zn containing alloy. This second region is in a three phase field lying mostly along the β'CuZn(5%Sn) and Sn (+2% Zn and 2% Cu) tie line with a minority of Cu<sub>6</sub>Sn<sub>5</sub><sup>21</sup>. In our case we expect a larger solubility of the Sn and Zn because here step (ii) is carried out at 350°C. The phases deduced from XRD and from this compositional analysis agree except for the Zn containing alloy. The discrepancy between the Cu<sub>5</sub>Zn<sub>8</sub> found by XRD compared to the β'CuZn(5%Sn) expected from compositional analysis could be due to the fact that our alloying occurred at 350°C instead of 250°C where the phase diagram was determined. In summary, phase 1 and therefore region 1 consists of Cu<sub>5</sub>Zn<sub>8</sub> and region 2 consists mainly of phase 2, Sn, surrounding small inclusions of phase 1.

In terms of phase composition, these results are consistent with previous literature<sup>11</sup>. However, the low magnification micrograph reveals that the segregated alloys reach a size of 10–20 μm, which is one order of magnitude larger than previously reported. Clearly the segregation of zinc and tin to such large length scales will impact the Kesterite growth.

In a multiphase system at chemical equilibrium, successive coarsening of the phases occurs as a result of the tendency of the system to decrease the interfacial area between them. This tendency is inversely proportional to the size of the domains, as described for nanoparticle metallurgy<sup>24</sup>. It also occurs in liquid emulsions, where it is driven by the reduction of surface tension, and is referred to as "Ostwald ripening"<sup>25</sup>. Although its thermodynamic driving force is normally lower compared to that of bulk alloy formation, it is non-negligible, as the phenomenon occurs at an appreciable rate leading to the 10–20 μm sized Cu<sub>5</sub>Zn<sub>8</sub> grains. In order to form the maximum Kesterite phase during the selenization step, tin and zinc need to diffuse over this length scale, otherwise the formation of the secondary phases ZnSe and Cu<sub>2</sub>SnSe<sub>3</sub> are expected respectively on the Sn-poor and Sn-rich areas.

To investigate this, the lateral elemental distribution at the area of interest was re-analyzed after selenization and compared with the metal alloy precursor. There is a noticeable change in the distribution of composition from bimodal and globally invariant Cu<sub>2</sub>/Zn ratio for the metallic alloy precursor to unimodal, with globally invariant Cu<sub>2</sub>/Sn ratio for the selenized absorber layer (figure 3a). This change in distribution is broadly explained by tin rich regions losing tin to zinc rich regions by either i) evaporation and condensation of SnSe<sup>27</sup> or ii) solid state diffusion. Most of the compositions in the area of interest are centred on the Kesterite composition (0.33 Cu<sub>2</sub> 0.33 Sn) with a tail of compositions along the Cu<sub>2</sub>ZnSnSe<sub>4</sub>–ZnSe

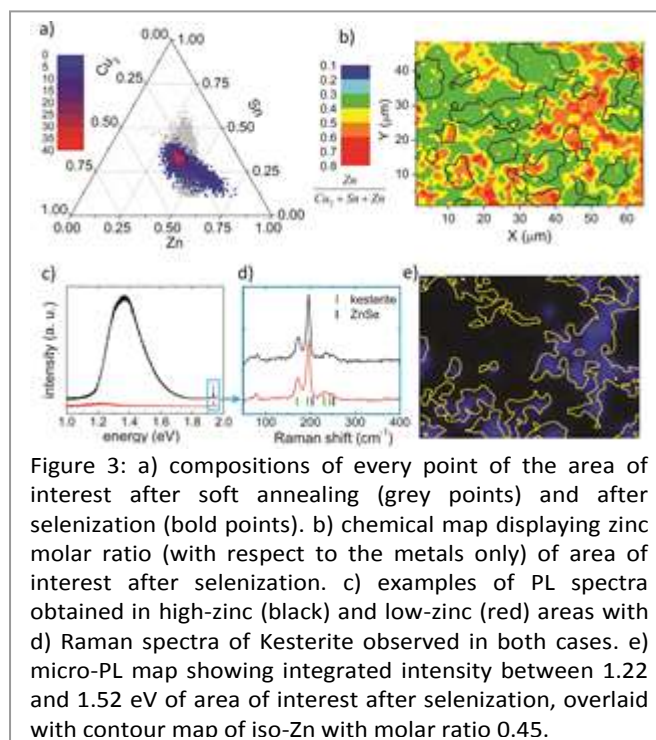


Figure 3: a) compositions of every point of the area of interest after soft annealing (grey points) and after selenization (bold points). b) chemical map displaying zinc molar ratio (with respect to the metals only) of area of interest after selenization. c) examples of PL spectra obtained in high-zinc (black) and low-zinc (red) areas with d) Raman spectra of Kesterite observed in both cases. e) micro-PL map showing integrated intensity between 1.22 and 1.52 eV of area of interest after selenization, overlaid with contour map of iso-Zn with molar ratio 0.45.

tie line. Figure 3b shows the Zn molar fraction over the position of interest. Cu<sub>2</sub> and Sn compositional maps are shown in the supporting information (figure S13). Essentially Kesterite should exist in areas where the zinc molar fraction is greater than 0.3, along with ZnSe in areas where the molar fraction is greater than 0.41<sup>27f</sup>. It can then be estimated that less than 3% of the area of interest has a composition where Cu<sub>2</sub>SnSe<sub>3</sub> could be present. The situation is consistent with the μ-PL/Raman measurements of the position of interest (figure 3c and d). The PL spectra were measured and integrated in the range 1.2–1.5 eV (figure 3c), which is the fingerprint region for doped ZnSe in Kesterite<sup>28</sup>, providing a PL map (figure 3d). A good agreement is observed between the PL map and regions of the selenized film with Zn molar ratio > 0.45. Examples of PL and Raman spectra from very low and very high ZnSe containing areas are shown in figure 3c. The Raman spectra confirm the presence of Kesterite in both areas. The fingerprint PL also shows that ZnSe is on or near the top surface, because otherwise, its luminescence emission would be absorbed by the < 1 eV band gap of Kesterite. This is confirmed by the SEM cross section analysis of a sister sample, showing a 500 nm thick ZnSe layer on top of the kesterite (figure S14 in supplementary information), which is similar to the microstructure observed in our previous publication and is also responsible for an overestimation of the molar ratio of Zn by EDS<sup>13</sup>.

An unexpected observation is that the location of ZnSe on the area of interest coincides more with the position of Sn-rich areas before selenization (falling outside the black contour lines on map 3.b). Quantitatively, 56% of the formerly Sn rich region 2 contains ZnSe compared to only 41% of the formerly Zn rich region 1<sup>27</sup>.

The greater presence of ZnSe in regions which were initially

tin rich could be explained either by the evaporation of tin as SnSe or by the different kinetics of selenization of the elements. Evaporation of SnSe would leave the area deficient in Sn with respect to stoichiometric Kesterite, thus leaving Cu<sub>2</sub>Se and ZnSe as secondary phases. Alternatively, we speculate that SnSe creates a diffusion barrier on the Sn surface, hindering the selenization of this metal. This implies that the Sn-poor areas of the precursor selenize faster. Subsequently, metallic Sn would diffuse from Sn-rich areas to form Kesterite in initially Zn-rich areas. Ultimately, the areas that were initially Sn-rich would be left with an excess of Zn, and thus appear as rich of ZnSe. Evidence for this can be found in the work of Fairbrother et al. and Dale et al., where Cu and Zn are the first elements to be sulfurized / selenized<sup>29,30</sup>, despite the Gibbs free energy of formation being more favourable for Sn(S,Se) compared to Cu<sub>2</sub>(S,Se) and Cu(S,Se)<sup>31</sup>. However, the rates at which metals are converted into chalcogenides can be kinetically controlled<sup>32</sup> which links to the broader concept of non-linear free energy relationship<sup>33,34</sup>.

This study shows that a simple marking technique allows ex-situ analyses in the same area of interest before and after critical synthesis steps. This approaches the advantages of in-situ analysis for situations where only ex-situ analyses are possible. The additional possibility to closely follow compositional changes at the micrometer scale gives valuable insights on chemical transformations, which is essential for the understanding of multinary compound formations. Here we focused on Cu<sub>2</sub>ZnSnSe<sub>4</sub> formation by selenization of metallic Cu-Sn-Zn films. We were able to conclude that the extent of metal alloy segregation occurring during a heating step affects significantly the extent of secondary phase segregation in the selenized Kesterite film. Counter-intuitively, ZnSe appears to segregate preferentially on areas formerly poor of Zn. Reducing the physical size of the metal alloys formed should reduce secondary phase formation and improve device efficiency.

## Notes and references

† Kesterite phase diagram of Choubrac et al. was measured for Kesterite samples sintered and annealed at 750 °C and cooled down at 50 °C/h.

‡‡ The EU seventh framework programme FP7/2007-2013 is acknowledged for funding through the Grant no. 284486. The authors express sincere thanks to Prof. Susanne Siebentritt (University of Luxembourg) for the constructive feedback.

- J.-M. Dubois and E. Belin-Ferre, Eds., *Wiley: Complex Metallic Alloys: Fundamentals and Applications*, Wiley-VCH.
- A. Fairbrother, M. Dimitrievska, Y. Sánchez, V. Izquierdo-Roca, A. Pérez-Rodríguez and E. Saucedo, *J. Mater. Chem. A*, 2015, **3**, 9451–9455.
- R. Moss, E. Tzimas, P. Willis, J. Arendorf, L. Espinoza, A. Chapman, N. Morley, E. Sims, R. Bryson, J. Pearson, F. Marscheider-Weidemann, M. Soulier, A. Lüllmann, C. Sartorius and K. Ostertag, *Critical metals in the path towards the decarbonisation of the EU energy sector*, Joint Research Centre, Institute for Energy and Transport, Luxembourg, 2013.
- W. Wang, M. T. Winkler, O. Gunawan, T. Gokmen, T. K. Todorov, Y. Zhu and D. B. Mitzi, *Advanced Energy Materials*, 2013, **4**, 1301465.
- D. Colombara, P. J. Dale, J. J. Scragg, S. Siebentritt and L. M. Peter, in *Advanced Concepts in Photovoltaics*, eds. A. J. Nozik, G. Conibeer, M. C. Beard, F. Schüth, T. S. Zhao, L. M. Peter and H. Frei, Royal Society of Chemistry, Cambridge, 2014.
- B. M. Başol, *IEEE Transactions on electron devices*, 1990, **37**, 418.
- M. Nakamura, N. Yoneyama, K. Horiguchi, Y. Iwata, K. Yamaguchi, H. Sugimoto and T. Kato, in *Photovoltaic Specialist Conference (PVSC), 2014 IEEE 40th*, 2014, pp. 0107–0110.
- D. G. Moon, J. H. Yun, J. Gwak, S. Ahn, A. Cho, K. Shin, K. Yoon and S. Ahn, *Energy Environ. Sci.*, 2012, **5**, 9914–9921.
- M. U. and Y. T. and T. M. and T. S. and H. A. and R. Maekawa, *Applied Physics Express*, 2013, **6**, 45501.
- S. Ahmed, K. B. Reuter, O. Gunawan, L. Guo, L. T. Romankiw and H. Deligianni, *Advanced Energy Materials*, 2011, **2**, 253–259.
- M. Arasimowicz, M. Thevenin and P. J. Dale, in *Materials Research Society Spring Meeting*, 2013, vol. 1538, pp. 123–129.
- L. Vauche, L. Risch, Y. Sánchez, M. Dimitrievska, M. Pasquinnelli, T. Goislard de Monsabert, P.-P. Grand, S. Jaime-Ferrer and E. Saucedo, *Progress in Photovoltaics: Research and Applications*, 2015, n/a–n/a.
- D. Colombara, E. V. C. Robert, A. Crossay, A. Taylor, M. Guennou, M. Arasimowicz, J. C. B. Malaquias, R. Djemour and P. J. Dale, *Solar Energy Materials and Solar Cells*, 2014, **123**, 220–227.
- Y. Wu and P. Yang, *Journal of the American Chemical Society*, 2001, **123**, 3165–3166.
- F. Panciera, Y.-C. Chou, M. C. Reuter, D. Zakharov, E. A. Stach, S. Hofmann and F. M. Ross, *Nat Mater*, 2015, **14**, 820–825.
- F. M. Ross, *Reports on Progress in Physics*, 2010, **73**, 114501.
- R. Schurr, A. Hölzing, S. Jost, R. Hock, T. Voß, J. Schulze, A. Kirbs, A. Ennaoui, M. Lux-Steiner, A. Weber, I. Kötschau and H. W. Schock, *Thin Solid Films*, 2009, **517**, 2465–2468.
- A. Weber, R. Mainz, T. Unold, S. Schorr and H.-W. Schock, *Physica Status Solidi (c)*, 2009, **6**, 1245–1248.
- J. C. Meier, I. Katsounaros, C. Galeano, H. J. Bongard, A. A. Topalov, A. Kostka, A. Karschin, F. Schuth and K. J. J. Mayrhofer, *Energy & Environmental Science*, 2012, **5**, 9319–9330.
- J. K. Larsen, L. Gütay and S. Siebentritt, *Applied Physics Letters*, 2011, **98**, 201910.
- Y. Huang, S. Chen, C. Chou and W. Gierlotka, *Journal of Alloys and Compounds*, 2009, **477**, 283–290.
- F. Jiang, S. Ikeda, T. Harada and M. Matsumura, *Advanced Energy Materials*, 2013, **4**, 1301381.
- F. Jiang, S. Ikeda, Z. Tang, T. Minemoto, W. Septina, T. Harada and M. Matsumura, *Prog. Photovolt: Res. Appl.*, 2015, n/a–n/a.
- W. Pfeiler, Ed., *Alloy Physics: A Comprehensive Reference*, Wiley-VCH.
- F. W. Ostwald, *Lehrbuch der Allgemeinen Chemie*, Engelmann, Leipzig, 1896, vol. 2.
- A. Redinger, D. M. Berg, P. J. Dale and S. Siebentritt, *Journal of the American Chemical Society*, 2011, **133**, 3320–3323.
- L. Choubrac, A. Lafond, M. Paris, C. Guillot-Deudon and S. Jobic, *Physical chemistry chemical physics: PCCP*, 2015, **17**, 15088–92.
- R. Djemour, M. Mousel, A. Redinger, L. Gütay, A. Crossay, D. Colombara, P. Dale and S. Siebentritt, *Applied Physics Letters*, 2013, **102**, 222108.
- A. Fairbrother, X. Fontané, V. Izquierdo-Roca, M. Espíndola-Rodríguez, S. López-Marino, M. Placidi, L. Calvo-Barrio, A. Pérez-Rodríguez and E. Saucedo, *Solar Energy Materials and Solar Cells*, 2013, **112**, 97–105.
- P. J. Dale, M. Arasimowicz, D. Colombara, A. Crossay, E. Robert and A. A. Taylor, *Materials Research Society*, 2013, vol. 1538.

- 31 J. J. Scragg, P. J. Dale, D. Colombara and L. M. Peter, *ChemPhysChem*, 2012, **13**, 3035–3046.
- 32 D. Colombara, L. M. Peter, K. D. Rogers and K. Hutchings, *Journal of Solid State Chemistry*, 2012, **186**, 36–46.
- 33 L. P. Hammett, *Journal of the American Chemical Society*, 1937, **59**, 96–103.
- 34 D. A. Sverjensky and P. A. Molling, *Nature*, 1992, **356**, 231–234.